


ac polarizability and photoionization-cross-section measurements in an optical lattice

Ryan Cardman^{Ⓧ,*,†}, Xiaoxuan Han^{*,‡}, Jamie L. MacLennan^{*}, Alisher Duspayev[Ⓧ], and Georg Raithel
 Department of Physics, University of Michigan, Ann Arbor, Michigan 48109, USA

 (Received 20 July 2021; revised 7 October 2021; accepted 22 November 2021; published 8 December 2021)

We use double-resonant two-photon laser spectroscopy to measure the dynamic scalar polarizability of the rubidium $5D_{3/2}$ level, $\alpha_{5D_{3/2}}^S$, at a wavelength of $\lambda = 1064$ nm. Since λ is shorter than the photoionization (PI) limit of the Rb $5D_{3/2}$ level, this state undergoes significant broadening due to PI. The 1064-nm field is applied in the form of a deep optical lattice ($\sim 10^5$ photon recoils) generated by an in-vacuum field-enhancement cavity. In our spectroscopic method, we use known dynamic polarizabilities to eliminate the need to measure the light intensity. Our method yields, in atomic units, $\alpha_{5D_{3/2}}^S = -524(17)$, in agreement with estimates. Additionally, we extract the $5D_{3/2}$ photoionization cross section σ at 1064 nm from spectral linewidths; we find $\sigma = 44(1)$ Mb.

DOI: [10.1103/PhysRevA.104.063304](https://doi.org/10.1103/PhysRevA.104.063304)

For some time, neutral atoms have been trapped by off-resonant optical fields for the purpose of redefining the second with unparalleled precision [1], simulating theoretical models [2–4], and constructing quantum computing protocols [5,6]. An atom in an electric field with a frequency far from resonance of an electric-dipole transition undergoes an energy shift due to the ac Stark effect, which is proportional to the field intensity. In applications of optical-dipole traps in optical clocks and in spectroscopy, differential ac Stark shifts of the relevant atomic states must be either very well known or eliminated using carefully determined “magic” wavelengths [7–9]. The ac shifts follow $\Delta W = -\alpha(\omega_L)E_L^2/4$, with a laser electric field E_L and angular frequency ω_L , and state-dependent dynamic polarizabilities α . Following the intensity-gradient force on the atomic center-of-mass (CM) coordinate, $-\nabla_{\mathbf{R}}\Delta W(\mathbf{R})$, states with positive (negative) α are attracted to (repelled from) locations of high field intensity. Also, the ac shifts of spectral lines of atomic transitions scale with the difference between the α -values of the relevant states.

For an atomic state $|n, l, j, m_j\rangle$ in a field with polarization unit vector $\hat{\epsilon}$, the dynamic polarizability is

$$\begin{aligned} \alpha_{n,l,j,m_j}(\omega_L) = & \frac{2}{\hbar} \left[\sum_{n',l',j',m'_j} |\langle n', l', j', m'_j | \hat{\epsilon} \cdot \hat{\mathbf{d}} | n, l, j, m_j \rangle|^2 \right. \\ & \times \frac{\omega_{nlj}^{n'l'j'}}{(\omega_{nlj}^{n'l'j'})^2 - \omega_L^2} + \text{p.v.} \sum_{l',j',m'_j} \int_0^\infty d\epsilon' \rho(\epsilon') \\ & \left. \times |\langle \epsilon', l', j', m'_j | \hat{\epsilon} \cdot \hat{\mathbf{d}} | n, l, j, m_j \rangle|^2 \frac{\omega_{nlj}^{\epsilon'}}{(\omega_{nlj}^{\epsilon'})^2 - \omega_L^2} \right], \end{aligned} \quad (1)$$

where $\hat{\mathbf{d}}$ is the electric-dipole moment operator, $\omega_{nlj}^{n'l'j'} = (W_{n'l'j'} - W_{nlj})/\hbar$ for bound state energies W_{nlj} and $W_{n'l'j'}$, and $\omega_{nlj}^{\epsilon'} = (\epsilon' - W_{nlj})/\hbar$ for free-electron-state (FES) energies ϵ' . The quantity $\rho(\epsilon')$ is the density of FESs with energy ϵ' and is equal to 1 per unit energy, for energy-normalized states [10]. When the photon energy $\hbar\omega_L$ is large enough to photoionize the atom, the integral term in Eq. (1) includes a pole at $\omega_L = \omega_{nlj}^{\epsilon'}$, with the real-valued principal integral yielding the FES polarizability contribution. In the high-frequency limit, $\omega_L > |\omega_{nlj}^{n'l'j'}|$ for all $|n', l', j', m'_j\rangle$, and in certain cases discussed in the Appendix, the polarizability approaches the free-electron polarizability, $\alpha_e = -1/\omega_L^2$ [11]. The free-electron polarizability follows from Eq. (1) by taking the limit $\omega_L \rightarrow \infty$ and using the Thomas-Reiche-Kuhn sum rule; it becomes even more apparent when evaluating the polarizability in the velocity gauge of the field [12]. The free-electron polarizability manifests, for instance, in the near-free-electron ponderomotive shift of bound Rydberg energy levels [13,14]. In a treatment beyond Eq. (1), an imaginary part arises [11] that is proportional to the PI cross section, which follows from the transition matrix element into the resonant FES [10].

In a linearly polarized field, the m_j -dependent polarizabilities $\alpha_{n,l,j,m_j}(\omega_L)$ depend on m_j -independent scalar and tensor polarizabilities, $\alpha_{n,l,j}^S(\omega_L)$ and $\alpha_{n,l,j}^T(\omega_L)$,

$$\alpha_{n,l,j,m_j}(\omega_L) = \alpha_{n,l,j}^S(\omega_L) + \frac{3m_j^2 - j(j+1)}{j(2j-1)} \alpha_{n,l,j}^T(\omega_L), \quad (2)$$

where the second term vanishes for $j < 1$. Otherwise, $\alpha_{n,l,j}^S$ and $\alpha_{n,l,j}^T$ follow from α_{n,l,j,m_j} -values computed for different $|m_j\rangle$. A third term, proportional to the vector polarizability $\alpha_{n,l,j}^V(\omega_L)$, is added to Eq. (2) only when the field polarization is not linear. Precision measurements of the dynamic polarizability have been conducted in various contexts, from dysprosium cooling and trapping with a 1064-nm dipole trap [15] to blackbody shifts in optical lattice clocks [16].

*These authors contributed equally to this work.

[†]rcardman@umich.edu

[‡]Present address: Department of Physics, Taiyuan Normal University, Jinzhong 030619, People's Republic of China.

In the present study, we measure $\alpha_{5D_{3/2}}^S$ for rubidium in an optical lattice of laser wavelength $\lambda = 1064$ nm. Its photon energy hc/λ suffices to photoionize $5D_{3/2}$ -atoms trapped in the optical lattice, in addition to contributing to the polarizability via the FES-term in Eq. (1). While no theoretical or experimental estimate has been made for the $5D_{3/2}$ dynamic polarizability, the static polarizabilities have been investigated [17–20], as well as the dynamic polarizability at 778.1 nm for $5D_{5/2}$ [21]. Because polarizabilities are related to fundamental atomic properties such as dipole matrix elements and van-der-Waals coefficients, measurements are of broad value and may also be useful for testing sophisticated atomic structure calculations.

Photoionization (PI), which affects astrophysical [22,23] and ultracold plasmas [24] that have recently been under study, also broadens the Rb $5D_{3/2}$ -levels in a 1064-nm field, as estimates based on measured Rb $5D_{5/2}$ [25] and calculated [25,26] Rb $5D$ PI cross sections show. These estimates exhibit that the PI-induced level broadening at 1064 nm is on the same order of magnitude as the ac Stark shift. Rb $5D$ -atoms prepared in a 1064-nm optical lattice, therefore, offer an excellent opportunity to measure both the dynamic scalar polarizability and the PI cross section of an atomic state in a single spectroscopic measurement, which we present here. While previous PI cross-section measurements have typically used the saturation technique or the trap loss/loading technique [27], which suffer from calibration uncertainties in the photoionizing light intensity and atom numbers, our method circumvents these difficulties, affording greater precision in the measurement.

From an applications point of view, the Rb $5D$ states are appealing to study for several reasons. First, there has been continued interest ranging from earlier decades [28–30] to recent years [31–33] in using the strong and narrow (natural linewidth <1 MHz) two-photon transition $5S_{1/2} \rightarrow 5D_J$ as an optical frequency reference, which necessitates precise calculation or cancellation of the relevant light shifts [21,34]. This two-photon transition’s wavelength (778 nm) can be directly generated by a semiconductor laser, or via second-harmonic generation of a laser at 1556 nm, which falls within the telecommunication band. Furthermore, the $5S_{1/2} \rightarrow 5D_{5/2}$ transition is one of the transitions recommended by the Consultative Committee of Length (CCL) for the practical definition of the meter [35].

The main components of the apparatus, atomic energy levels, and optical beam geometries are exhibited in Fig. 1. We load ^{85}Rb atoms from a magneto-optical trap, initially prepared in the $F = 3$ ground-state hyperfine level, into the near-perfect TEM_{00} mode of a near-concentric field-enhancement cavity with a finesse of ≈ 600 at $\lambda = 1064$ nm [36]; the cloud of atoms is cooled in the geometric center of the cavity where the optical lattice is focused [37–39]. After loading, the lattice is adiabatically ramped to a maximum depth of $\sim 10^5 E_r$, where $E_r = h \times 2.076$ kHz is the photon recoil for ^{85}Rb at 1064 nm. To observe the lattice-shifts affecting the D1 line, we pulse a 795-nm probe laser for a duration of ~ 15 μs and scan it from -36 to 1344 MHz with respect to the frequency of the $|5S_{1/2}, F = 3\rangle \rightarrow |5P_{1/2}, F' = 2\rangle$ transition. A copropagating 762-nm probe laser is pulsed on for ~ 500 ns

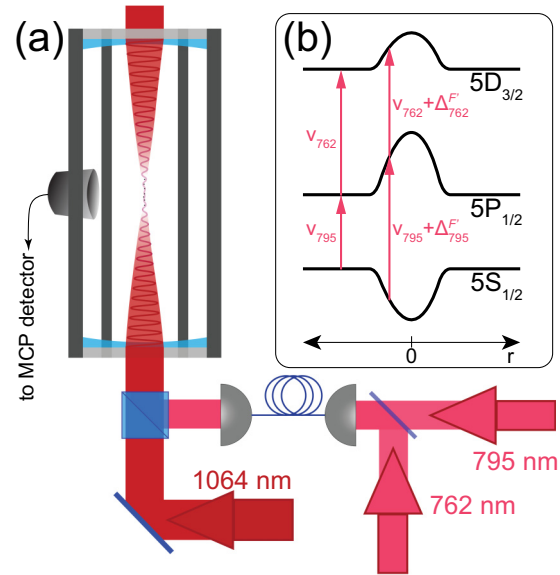


FIG. 1. (a) Sketch of the experimental apparatus, and (b) energy level diagram with outlined ac Stark shifts for atoms on the standing-wave antinodes as a Gaussian function of radial position transverse to the longitudinal axis of the 1064 nm optical lattice (not to scale).

and is independently scanned from 57 to -843 MHz with respect to the lattice-field-free frequency difference between the $|5P_{1/2}, F' = 2\rangle$ and $|5D_{3/2}, F'' = 3\rangle$ states. Lattice-induced PI of atoms excited into $5D_{3/2}$ yields a count of atoms in this state when the resulting ions are guided onto a microchannel plate detector (MCP) with an extraction voltage. This procedure yields a two-dimensional map of ion counts as a function of the two probe laser frequencies, as shown in Fig. 2(a).

In Fig. 2(a) we display ion counts as a function of the frequencies of both probe lasers. The figure exhibits two diagonally aligned branches of $5D_{3/2}$ atomic signals. The branches correspond to the intermediate hyperfine states $F' = 2$ and 3, which present two pathways through which the atoms can be excited into $5D_{3/2}$ via stepwise, double-resonant, two-photon excitation. For the two pathways $F' = 2$ and 3, we define detunings $\Delta_{795}^{F'}$ and $\Delta_{762}^{F'}$ of the excitation lasers from their respective lattice-field-free resonances [see Fig. 1(b) and the axis insets in Fig. 2(a)].

The ac shifts evident from the slopes of the signal branches in Fig. 2 are caused by the dynamic polarizabilities of all relevant atomic states, $5S_{1/2}, F = 3$, $5P_{1/2}, F' = 2$ or 3, and $5D_{3/2}, F'' = 1-4$. At lattice depths of $\sim 10^5$ photon recoils, this ac Stark shift actually splits the $5D_{3/2}$ into 12 lines corresponding to the product spaces of quantum numbers $|m_j|$ and m_l for nuclear spin $I = 5/2$, but the significant broadening brought on by the large PI cross section for $5D_{3/2}$ completely masks this effect in our study [38,40]. For the ground- and intermediate-state polarizabilities at 1064 nm, we use the theoretical values $\alpha_{5S_{1/2}}^S = 687.3(5)$ [41] and $\alpha_{5P_{1/2}}^S = -1226(18)$ [40] (in atomic units and applicable to all hyperfine sublevels). The objective of the measurement then is, in principle, to extract the scalar and tensor polarizabilities, $\alpha_{5D_{3/2}}^S$ and $\alpha_{5D_{3/2}}^T$, from the slopes of the signal branches in Fig. 2. From an estimate given below, it is predicted that the magnitude of $\alpha_{5D_{3/2}}^T$

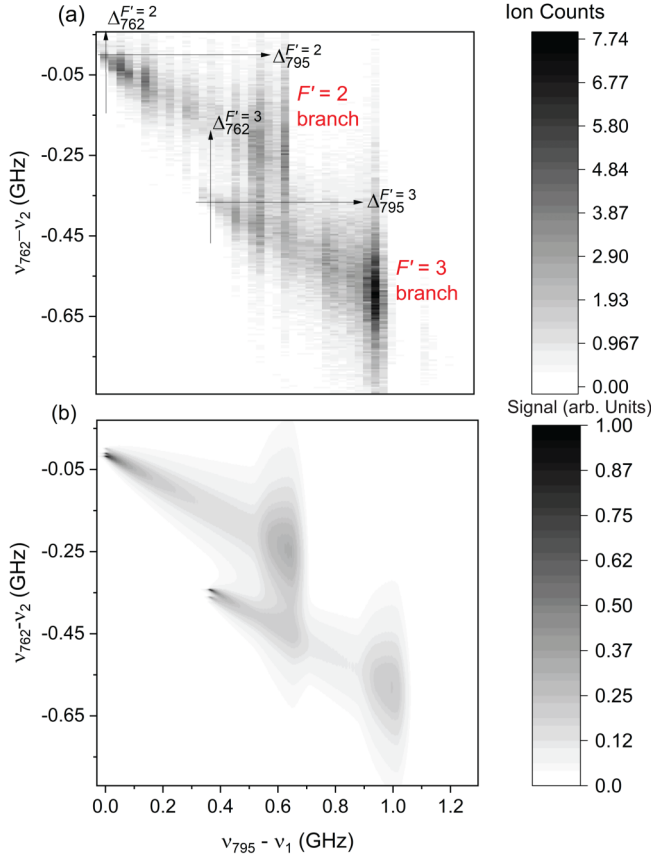


FIG. 2. (a) Results of two-photon spectroscopy as a function of 795- and 762-nm probe laser frequencies (ν_{795} and ν_{762} , respectively). The reference frequencies ν_1 and ν_2 correspond to splittings between the lattice-field-free $5S_{1/2}$, $F = 3$ and $5P_{1/2}$, $F' = 2$ levels, and between the lattice-field-free $5P_{1/2}$, $F' = 2$ and $5D_{3/2}$, $F'' = 3$ levels, respectively. Data are averaged over 30 experimental cycles. (b) Numerical simulation (see the Supplemental Material [51]) for input parameters $\alpha_{5D_{3/2}}^S = -524$, $\alpha_{5D_{3/2}}^T = 0$, and $\sigma = 40$ Mb.

is at or below the level of uncertainty of the experimental method. In the following, we therefore restrict our analysis to the case $\alpha_{5D_{3/2}}^T = 0$.

The two signal branches in Fig. 2 yield two measurements for the slopes, $d\Delta_{762}^{F'}/d\Delta_{795}^{F'}$, associated with the two intermediate states $5P_{1/2}$, $F' = 2$ and $5P_{1/2}$, $F' = 3$. The scalar polarizability $\alpha_{5D_{3/2}}^S$ then follows from

$$\alpha_{5D_{3/2}}^S(F') = \alpha_{5P_{1/2}}^S - \frac{d\Delta_{762}^{F'}}{d\Delta_{795}^{F'}} (\alpha_{5S_{1/2}}^S - \alpha_{5P_{1/2}}^S). \quad (3)$$

This measurement method is similar to a method used in [38]. Because Fig. 2(a) yields two readings for the slope $d\Delta_{762}^{F'}/d\Delta_{795}^{F'}$, we obtain two measurements for $\alpha_{5D_{3/2}}^S$ that correspond with the intermediate hyperfine pathways $F' = 2$ and 3. The method is self-calibrating in the sense that a direct measurement of the lattice intensity in the atomic sampling region is unnecessary.

The experimental data are acquired by scanning the detuning of the 762-nm laser, $\nu_{762} - \nu_2$, for a set of values for the detuning $\nu_{795} - \nu_1$ of the 795-nm laser. A vertical slice of

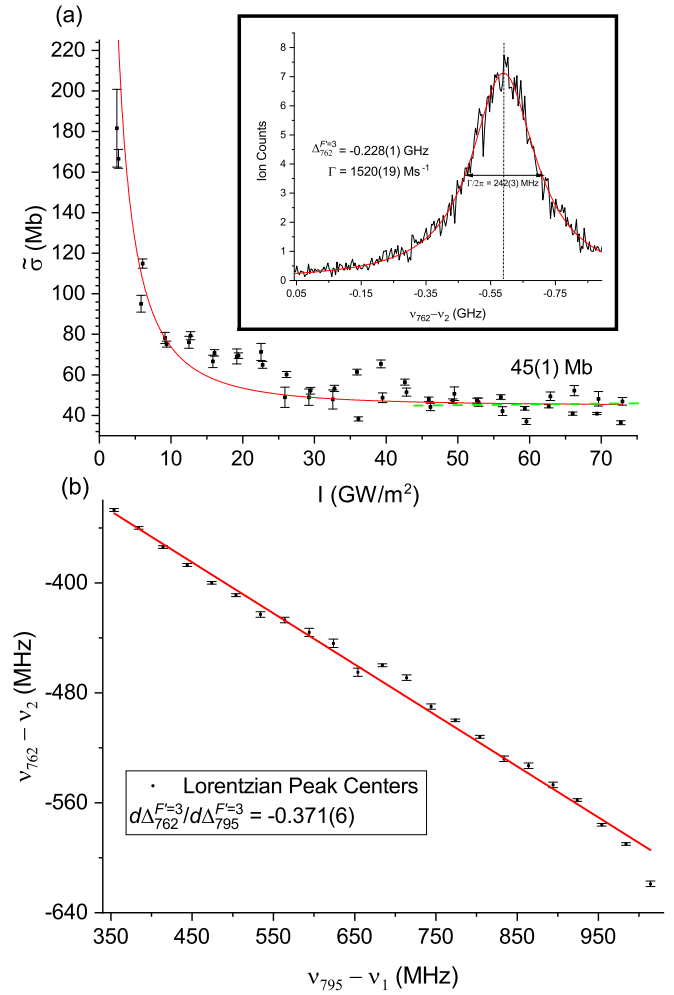


FIG. 3. (a) σ vs I at the atoms' locations. The data and a fit result depicted in red yield a $5D_{3/2}$ photoionization cross section of $\sigma = 45(1)$ Mb. The inset shows a typical spectral peak [a single, vertical slice from Fig. 2(a)] characterized by the 762-nm laser detuning at a fixed 795-nm frequency setting ($\nu_{795} - \nu_1 = 0.984$ GHz), along with Γ and $\Delta_{762}^{F'=3}$ obtained from its Lorentzian fitting parameters. We average ion counts over 30 experimental cycles. (b) Lorentzian peak centers in $\nu_{762} - \nu_2$ and their uncertainties vs $\nu_{795} - \nu_1$ for the $F' = 3$ signal branch in Fig. 2(a). The slope of the weighted linear fit to these data is $d\Delta_{762}^{F'=3}/d\Delta_{795}^{F'=3} = -0.371(6)$. We repeat this procedure for the $F' = 2$ branch.

the map in Fig. 2(a) at a value of $\nu_{795} - \nu_1 = 0.984$ GHz is provided in the inset of Fig. 3(a) as an example. We find that the spectral lines along each frequency setting of the 795-nm laser follow near-perfect Lorentzian shapes, down to the noise level several linewidths away from the line centers. This observation serves as experimental evidence that the line profiles are the result of a level decay mechanism, which in our case is the PI of the $5D_{3/2}$ levels. For each of the individual spectra at fixed $\nu_{795} - \nu_1$, we obtain the line centers and linewidths using Lorentzian fits. Depending on whether the signal has contributions from both signal branches $F' = 2$ and 3 in Fig. 2 or from just one, we employ double- or single-Lorentzian fits, respectively. The line centers yield two sets of data points $\Delta_{762}^{F'}$ ($\Delta_{795}^{F'}$) for $F' = 2$ and 3. We present the sets for the $F' = 3$ branch in Fig. 3(b). The slopes $d\Delta_{762}^{F'}/d\Delta_{795}^{F'}$ from

TABLE I. Summary of quantities used to extract $\alpha_{5D_{3/2}}^S$, as well as a summary of results (in atomic units).

Quantity	Value	Source
$\alpha_{5S_{1/2}}^S$	687.3(5)	[41] ^a
$\alpha_{5P_{1/2}}^S$	-1226(18)	[40]
$d\Delta_{762}^{F'=2}/d\Delta_{795}^{F'=2}$	-0.36(1)	Experimental data, this work
$d\Delta_{762}^{F'=3}/d\Delta_{795}^{F'=3}$	-0.371(6)	Experimental data, this work
$\alpha_{5D_{3/2}}^S (F' = 2)$	-537(27)	Eq. (3)
$\alpha_{5D_{3/2}}^S (F' = 3)$	-516(22)	Eq. (3)
$\alpha_{5D_{3/2}}^S$	-524(17)	Weighted average

^aPrevious calculations and measurements are found in [11,42–45].

respective weighted linear fits yield a pair of measured values of $\alpha_{5D_{3/2}}^S$ via Eq. (3). Essential inputs from other sources and our results are summarized in Table I. The uncertainties in the scalar polarizability measurements are dominated by the statistical errors of the linear fits and the given uncertainty in $\alpha_{5P_{1/2}}^S$. Systematic effects from stray electromagnetic fields, atomic collisions, and laser frequency linearity are negligible. The weighted average over the pair of measured dynamic scalar polarizabilities is $\alpha_{5D_{3/2}}^S = -524(17)$ atomic units.

Expanding upon previous results from other works, theoretical estimates for $\alpha_{5D_{3/2}}^S$ and $\alpha_{5D_{3/2}}^T$ can be obtained. We use the listings of energy levels [46], and of dipole matrix elements or contributions of transitions to other polarizabilities [44,47], to compile energies and matrix elements for the $5D_{3/2}$ and the perturber states ($n' \leq 7$) $F_{5/2}$ and ($n' \leq 8$) P_J required in the first term in Eq. (1). For the ($n' \geq 8$) $F_{5/2}$ and ($n' \geq 9$) P_J contributions, we use energy levels and dipole matrix elements from our own Rydberg-atom calculations [48], which employ model potentials given in [49]; values agree well with those from an online calculator [50]. We estimate the bound-bound contributions to the dynamic polarizabilities $\alpha_{5D_{3/2}}^S$ and $\alpha_{5D_{3/2}}^T$ at 1064 nm to be -540 and 16, respectively. To estimate the continuum integral in Eq. (1), we compute bound-free matrix elements on a dense FES energy grid (spacing $\sim h \times 40$ GHz) over a range from $\epsilon' = 0$ up to ~ 20 eV, yielding continuum contributions of 19 for $\alpha_{5D_{3/2}}^S$ and -3 for $\alpha_{5D_{3/2}}^T$. The core contribution to $\alpha_{5D_{3/2}}^S$, not shown in Eq. (1), is estimated at a value of 9, provided in [21] for dc and for 778 nm. Our estimates for the scalar and tensor polarizabilities sum up to totals of $\alpha_{5D_{3/2}}^S = -511$ and $\alpha_{5D_{3/2}}^T = 13$. From our simulation described in the Supplemental Material [51], we estimate that the presence of a tensor polarizability of 13 would cause a positive shift of <10 in the deduced scalar polarizability when using Eq. (3). Therefore, we conclude that the estimated systematic uncertainty in $\alpha_{5D_{3/2}}^S$ related to the tensor polarizability lies within the uncertainty of ± 17 of the measurement value, $\alpha_{5D_{3/2}}^S = -524(17)$, reported in Table I.

In the following, we discuss a measurement of the $5D_{3/2}$ PI cross section. For a given detuning $\Delta_{795}^{F'}$, the 1064-nm light intensity I at the locations of atoms contributing to the peak in the ion signal in the F' branch is given by $I = 2h\Delta_{795}^{F'} c \epsilon_0 / (\alpha_{5S_{1/2}}^S - \alpha_{5P_{1/2}}^S)$, with an uncertainty arising from the polarizabilities and the natural linewidth of the rubidium

D1 line (5.75 MHz [52]). The linewidth of ion spectra for fixed $\Delta_{795}^{F'}$ and scanned $\Delta_{762}^{F'}$, $\Gamma/2\pi$, obtained from Lorentzian fits as shown in Fig. 3(a), then provides an upper limit of the PI decay rate Γ_{PI} at intensity I . Using

$$\Gamma_{PI} = \frac{\sigma I}{\hbar\omega_L} \quad (4)$$

for each measured decay rate $\Gamma(I)$, we obtain an upper bound $\tilde{\sigma}(I) = \hbar\omega_L \Gamma(I)/I$ for the Rb $5D_{3/2}$ PI cross section σ . For atoms located near the bottoms of the lattice wells, corresponding to the largest $\Delta_{795}^{F'}$ and the largest intensities I , the broadening is almost exclusively given by PI. In contrast, at the lowest $\Delta_{795}^{F'}$ and intensities I , other mechanisms, such as the excited-state hyperfine coupling and residual off-resonant two-photon signals, are principal. As a result, $\tilde{\sigma}(I) \approx \sigma$ at large I and $\tilde{\sigma}(I) \gg \sigma$ at low I . This effect is exhibited in Fig. 3(a), where the quantity $\tilde{\sigma}$ converges to σ (and Γ to Γ_{PI}) at the high-intensity end of the I -axis.

Quantitatively, we obtain σ from the data in Fig. 3(a) using two methods. In method A, we take the arithmetic average of $\tilde{\sigma}$ in the asymptotic region $I \gtrsim 45$ GW/m² and utilize the standard error of the mean as its uncertainty. Method A yields $\sigma = 45(1)$ Mb. In method B, we apply a fit function $\tilde{\sigma} = \sqrt{\sigma^2 + \gamma^2/I^2}$, where γ accounts for broadening mechanisms other than PI. This fit also gives $\sigma = 45(1)$ Mb. Combining the two methods, we have $\sigma = 45(1)$ Mb. Our simulations, explained in the Supplemental Material [51], show that the measurement method likely overestimates the PI cross section of an isotropic atom sample by $\approx 1.7\%$, leading to our slightly corrected final result of $\sigma = 44(1)$ Mb. Based on the good qualitative agreement of measured and simulated strength ratios between the $F' = 2$ and 3 signal bars in Fig. 2, where the atom sample in the simulation is isotropic, we do not believe that optical pumping causes a significant deviation of our measured PI cross section from what it would be under perfectly isotropic conditions.

In a calculation based on fine-structure-less model potentials from [49], we have found a total shell-averaged PI cross section of 32.4 Mb at 1064 nm and 43.7 Mb at the PI threshold wavelength, which is close to calculations in [25] and [26]. Trap-loss measurements in [25] for Rb $5D_{5/2}$ gave a result of 18 Mb at 1064 nm and an estimate of 25 Mb at threshold. The discrepancies between the results for the Rb $5D$ PI cross sections await a future explanation.

In summary, we have spectroscopically measured the dynamic scalar polarizability of the rubidium $5D_{3/2}$ state in a 1064 nm optical lattice using two probe lasers at 795 and 762 nm. We report $\alpha_{5D_{3/2}}^S = -524(17)$ and estimate $|\alpha_{5D_{3/2}}^T| \ll |\alpha_{5D_{3/2}}^S|$. The observed PI-induced line broadening has yielded a PI cross section of $\sigma = 44(1)$ Mb. Future experimental directions involve the measurement of $\alpha_{5P_{1/2}}^S$ with a Rydberg excitation field probing the 1064-nm lattice shifts of the intermediate $5P_{1/2}$ state and auxiliary Rydberg levels [38]. Our measurement will also aid in the preparation of recently predicted Rydberg-atom-ion molecules [55] and of novel high-angular-momentum Rydberg states in a deep, 1064-nm Rydberg-atom optical lattice [56,57] using stepwise excitation via an intermediate Rb $5D$ state. It would also be desirable to obtain theoretical estimates of $\alpha_{5D_{3/2}}^S$ and improved

theoretical values for σ to compare with experimental results. The system presented in this study involving different forces from the internal-state-dependent optical potentials acting on the atoms could furthermore be numerically investigated using the fewest switches surface hopping (FSSH) algorithm [58,59].

ACKNOWLEDGMENTS

This work was supported by NSF Grants No. PHY-1806809 and No. PHY-2110049. X.H. acknowledges support from the program of China Scholarships Council (No. 201808140193). We would like to thank Yun-Jhih Chen for initial experimental work.

APPENDIX

1. Contribution of bound-FES matrix elements to the dynamic polarizability

The expression in Eq. (1) for the dynamic polarizability of an electron in a bound atomic state includes a sum over bound-bound couplings and a continuum integral over FES, regardless of whether the laser wavelength is above or below the photoionization threshold. In this Appendix, we explore the contributions in Eq. (1) to the dynamic $5D_{3/2}$ polarizability as a function of laser wavelength.

For a Rb $5D_{3/2}$ atom in a 1064-nm optical field, the integrand under the FES term exhibits a singularity at a free-electron energy of $\epsilon' = \hbar\omega_L + W_{5D_{3/2}} = 0.17$ eV. This leads to an integrand of the form $f(\epsilon')/(\epsilon' - 0.17$ eV) with a function $f(\epsilon')$ that varies smoothly across the singularity (which is inside the integration range). Cauchy's principal value (p.v.) of the integral contributes to the ac polarizability and Stark effect. The pole also realizes an imaginary quantity proportional to the PI cross-section that broadens the atomic energy level [not exhibited in Eq. (1)]. The p.v. integral can be evaluated in a straightforward manner by numerical integration from $\epsilon' = 0$ to a large enough value for the p.v. integral to converge. Convergence is reached because the bound-free dipole moment drops off sufficiently fast.

In Fig. 4, we exhibit the contributions of the FES term to the scalar and tensor polarizabilities for the Rb $5D_{3/2}$ level over a wide range of the optical wavelength, $\lambda = 2\pi c/\omega_L$. At wavelengths longer than the PI wavelength, there is no pole in Eq. (1), and the contributions to the scalar and tensor polarizabilities asymptotically approach dc limits of 102 and -23 , respectively (off-scale to the right in Fig. 4). Adding FES and bound-bound contributions, we find the total scalar polarizabilities shown in Fig. 5. At short wavelengths, the FES contribution to the scalar polarizability is about half that of the bound-bound contribution, with both contributions adding up to the free-electron polarizability, $\alpha_e = -1/\omega_L^2$. The FES and bound-bound contributions to the tensor polarizability approximately cancel at short wavelengths.

The cusp behavior of the FES contribution near the PI threshold at 1250 nm, seen in Fig. 4, arises because in that case the pole is just inside or outside the integration range $\epsilon' > 0$. Due to the continuity of the energy-averaged oscillator strengths across the PI threshold, the cusp of the FES contribution at the PI threshold disappears upon adding FES and

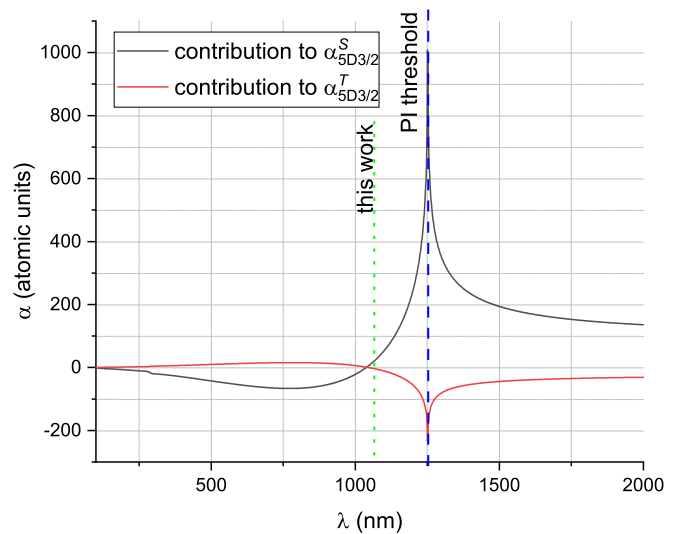


FIG. 4. Contributions of the FES term toward the Rb $5D_{3/2}$ dynamic polarizabilities over a range of wavelengths from above to below the PI threshold (indicated by dashed, blue line). The contribution to the scalar polarizability is indicated by the black curve, while the tensor is indicated by the red curve.

bound-bound contributions, as seen in Fig. 5. The divergences in Fig. 5 seen at wavelengths longer than the PI threshold are due to bound-bound resonances from $5D_{3/2}$ into Rydberg states.

2. Free-electron-polarizability approximation for the rubidium $5D_{3/2}$ level

The free-electron polarizability, $\alpha_e = -1/\omega_L^2$, characterizes the strength of the ponderomotive force acting on

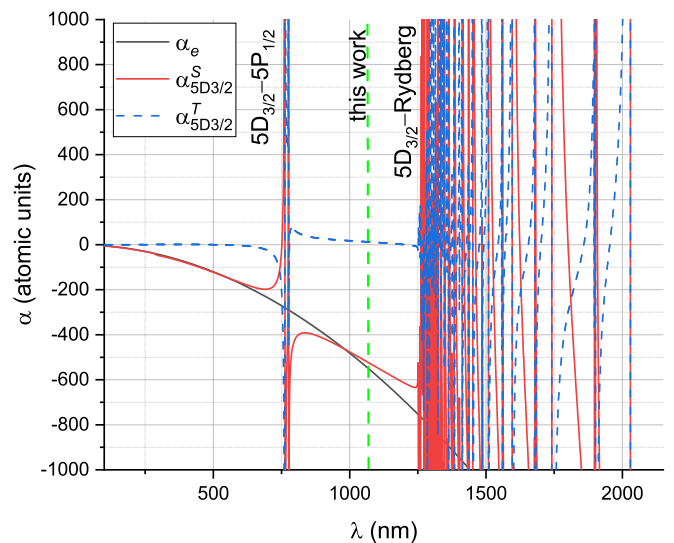


FIG. 5. Total Rb $5D_{3/2}$ dynamic scalar (red-solid) and tensor (blue-dashed) polarizability as a function of wavelength, neglecting the small and approximately constant core contribution. The free-electron polarizability α_e is also shown. The scalar and tensor polarizabilities at 1064 nm are on the green, dashed line. Resonances of electronic transitions to the $5P_{1/2}$ and Rydberg P_j - and F_j -states are indicated.

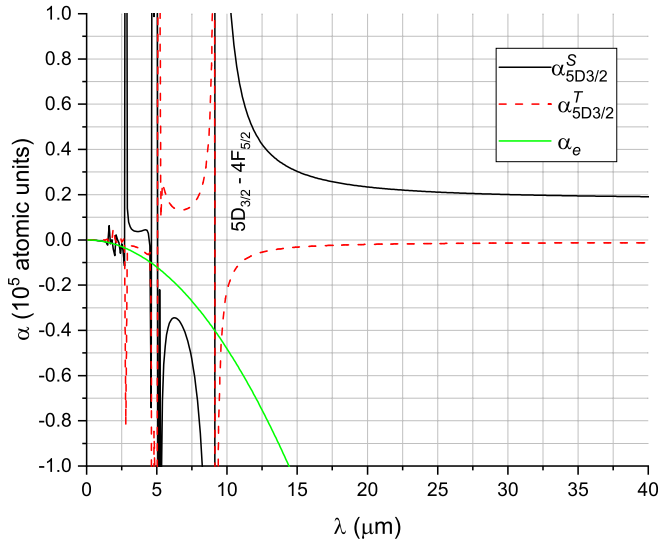


FIG. 6. Total dynamic scalar (black), tensor (red-dashed), and free-electron (green-solid) polarizabilities of the Rb $5D_{3/2}$ level at wavelengths stretching into the far-infrared (fir) regime. The resonance $5D_{3/2} \rightarrow 4F_{5/2}$ at $9 \mu\text{m}$ is indicated.

an electron [10] for short optical wavelengths. As can be seen in Fig. 5, α_e is a good approximation for the total Rb $5D_{3/2}$ dynamic scalar polarizability for wavelengths shorter than about 600 nm, while the tensor polarizability is near zero. This approximation for short-wavelength fields, discussed in depth in [12], arises from the following expansion:

$$\frac{\omega_{nlj}^{n'l'j'}}{(\omega_{nlj}^{n'l'j'})^2 - \omega_L^2} = -\omega_{nlj}^{n'l'j'}/\omega_L^2 \left[1 + \frac{(\omega_{nlj}^{n'l'j'})^2}{\omega_L^2} + \dots \right]. \quad (\text{A1})$$

When summed over all possible n', l', j', m'_j , the quantity $\omega_{nlj}^{n'l'j'} |\langle n', l', j', m'_j | \hat{\epsilon} \cdot \hat{\mathbf{d}} | n, l, j, m_j \rangle|^2$ approaches a constant per the Thomas-Reiche-Kuhn sum rule. For the Rb $5D_{3/2}$ level, this approximation breaks down for wavelengths longer than about 600 nm, where the downward $5D_{3/2} \rightarrow 5P_{1/2}$ coupling at 762 nm begins to cause substantial deviations from the free-electron behavior. At longer wavelengths, additional resonances due to upward couplings to F_j and other P_j states, including the Rydberg series, become dominant. It is somewhat coincidental that the dynamic scalar polarizability at 1064 nm is near the free-electron value $\alpha_e = -1/\omega_L^2 = -545$. Inspection of Fig. 5 shows that this is related to the fact that 1064 nm is about halfway in between the $5D_{3/2} \rightarrow 5P_{1/2}$ and the Rydberg resonances, whose effects approximately cancel at 1064 nm.

Interestingly, the polarizability of Rydberg atoms tends to equal the free-electron value, $\alpha_e = -1/\omega_L^2$, for wavelengths as long as into the mm range [13,14], despite the fact that Rydberg levels have bound-bound resonances across the ir, visible, and uv ranges. However, those resonances are weak and narrow, so that they are only significant at laser frequencies very close to one such resonance. Otherwise, the Rydberg-atom polarizability approximately equals $-1/\omega_L^2$, and is purely a scalar.

For completeness, in Fig. 6 it is shown that the polarizability of the $5D_{3/2}$ level in the far-infrared (fir) region behaves fundamentally differently from that of Rydberg levels. This is due to strong ir transitions from $5D_{3/2}$, most of all the $5D_{3/2} \rightarrow 4F_{5/2}$ resonance at $9 \mu\text{m}$. These have no equivalent for Rydberg levels. For $\lambda \rightarrow \infty$, the $5D_{3/2}$ scalar and tensor polarizabilities approach dc values of 18012 and -1093 (in our calculation), which include small bound-free contributions of 102 and -23 , respectively.

-
- [1] K. Beloy, M. I. Bodine, T. Bothwell, S. M. Brewer, S. L. Bromley, J.-S. Chen, J.-D. Deschênes, S. A. Diddams, R. J. Fasano, T. M. Fortier, Y. S. Hassan, D. B. Hume, D. Kedar, C. J. Kennedy, I. Khader, A. Koepke, D. R. Leibrandt, H. Leopardi, A. D. Ludlow *et al.* [Boulder Atomic Clock Optical Network (BACON) Collaboration], *Nature (London)* **591**, 564 (2021).
- [2] F. Le Kien, P. Schneeweiss, and A. Rauschenbeutel, *Eur. Phys. J. D* **67**, 92 (2013).
- [3] E. Guardado-Sanchez, P. T. Brown, D. Mitra, T. Devakul, D. A. Huse, P. Schauf, and W. S. Bakr, *Phys. Rev. X* **8**, 021069 (2018).
- [4] J. Hu, L. Feng, Z. Zhang, and C. Chin, *Nat. Phys.* **15**, 785 (2019).
- [5] M. Saffman, *J. Phys. B* **49**, 202001 (2016).
- [6] M. Morgado and S. Whitlock, *AVS Quantum Sci.* **3**, 023501 (2021).
- [7] M. S. Safronova, C. J. Williams, and C. W. Clark, *Phys. Rev. A* **67**, 040303(R) (2003).
- [8] V. V. Flambaum, V. A. Dzuba, and A. Derevianko, *Phys. Rev. Lett.* **101**, 220801 (2008).
- [9] N. Lundblad, M. Schlosser, and J. V. Porto, *Phys. Rev. A* **81**, 031611(R) (2010).
- [10] H. Friedrich, *Theoretical Atomic Physics* (Springer International, Cham, 2017).
- [11] N. L. Mankov and V. D. Ovsiannikov, *J. Phys. B* **10**, 569 (1977).
- [12] T. Topcu and A. Derevianko, *Phys. Rev. A* **88**, 042510 (2013).
- [13] S. K. Dutta, J. R. Guest, D. Feldbaum, A. Walz-Flannigan, and G. Raithel, *Phys. Rev. Lett.* **85**, 5551 (2000).
- [14] S. E. Anderson, K. C. Younge, and G. Raithel, *Phys. Rev. Lett.* **107**, 263001 (2011).
- [15] C. Ravensbergen, V. Corre, E. Soave, M. Kreyer, S. Tzanova, E. Kirilov, and R. Grimm, *Phys. Rev. Lett.* **120**, 223001 (2018).
- [16] J. A. Sherman, N. D. Lemke, N. Hinkley, M. Pizzocaro, R. W. Fox, A. D. Ludlow, and C. W. Oates, *Phys. Rev. Lett.* **108**, 153002 (2012).
- [17] V. A. Davydkin and B. A. Zon, *Opt. Spectrosc.* **52**, 359 (1982).
- [18] A. A. Kamenski and V. D. Ovsiannikov, *J. Phys. B* **39**, 2247 (2006).
- [19] D. A. Kondrat'ev, I. L. Beigman, and L. A. Vainshtein, *Bull. Lebedev Phys. Inst.* **35**, 355 (2008).

- [20] S. Snigirev, A. Golovizin, D. Tregubov, S. Pyatchenkov, D. Sukachev, A. Akimov, V. Sorokin, and N. Kolachevsky, *Phys. Rev. A* **89**, 012510 (2014).
- [21] K. W. Martin, B. Stuhl, J. Eugenio, M. S. Safronova, G. Phelps, J. H. Burke, and N. D. Lemke, *Phys. Rev. A* **100**, 023417 (2019).
- [22] P. S. Barklem, *Astron. Astrophys. Rev.* **24**, 9 (2016).
- [23] L. Zhao, W. Eissner, S. N. Nahar, and A. K. Pradhan, [arXiv:1801.02188](https://arxiv.org/abs/1801.02188).
- [24] T. K. Langin, G. M. Gorman, and T. C. Killian, *Science* **363**, 61 (2019).
- [25] B. C. Duncan, V. Sanchez-Villicana, P. L. Gould, and H. R. Sadeghpour, *Phys. Rev. A* **63**, 043411 (2001).
- [26] M. Aymar, O. Robaux, and S. Wane, *J. Phys. B* **17**, 993 (1984).
- [27] T. P. Dinneen, C. D. Wallace, K.-Y. N. Tan, and P. L. Gould, *Opt. Lett.* **17**, 1706 (1992).
- [28] F. Nez, F. Biraben, R. Felder, and Y. Millerioux, *Opt. Commun.* **102**, 432 (1993).
- [29] D. Touahri, O. Acef, A. Clairon, J.-J. Zondy, R. Felder, L. Hilico, B. de Beauvoir, F. Biraben, and F. Nez, *Opt. Commun.* **133**, 471 (1997).
- [30] L. Hilico, R. Felder, D. Touahri, O. Acef, A. Clairon, and F. Biraben, *Eur. Phys. J. J.* **4**, 219 (1998).
- [31] O. Terra and H. Hussein, *Appl. Phys. B* **122**, 27 (2016).
- [32] K. D. Rathod and V. Natarajan, *Sci. and Cult.* **83**, 39 (2017).
- [33] K. W. Martin, G. Phelps, N. D. Lemke, M. S. Bigelow, B. Stuhl, M. Wojcik, M. Holt, I. Coddington, M. W. Bishop, and J. H. Burke, *Phys. Rev. Appl.* **9**, 014019 (2018).
- [34] V. Gerginov and K. Beloy, *Phys. Rev. Appl.* **10**, 014031 (2018).
- [35] T. J. Quinn, *Metrologia* **40**, 103 (2003).
- [36] A. E. Siegman, *Lasers* (University Science Books, Mill Valley, 1986).
- [37] Y.-J. Chen, S. Zigo, and G. Raithel, *Phys. Rev. A* **89**, 063409 (2014).
- [38] Y.-J. Chen, L. F. Gonçalves, and G. Raithel, *Phys. Rev. A* **92**, 060501(R) (2015).
- [39] J. L. MacLennan, Y.-J. Chen, and G. Raithel, *Phys. Rev. A* **99**, 033407 (2019).
- [40] A. Neuzner, M. Körber, S. Dürr, G. Rempe, and S. Ritter, *Phys. Rev. A* **92**, 053842 (2015).
- [41] B. Arora and B. K. Sahoo, *Phys. Rev. A* **86**, 033416 (2012).
- [42] K. D. Bonin and M. A. Kadar-Kallen, *Phys. Rev. A* **47**, 944 (1993).
- [43] M. Marinescu, H. R. Sadeghpour, and A. Dalgarno, *Phys. Rev. A* **49**, 5103 (1994).
- [44] M. S. Safronova, C. J. Williams, and C. W. Clark, *Phys. Rev. A* **69**, 022509 (2004).
- [45] M. S. Safronova, B. Arora, and C. W. Clark, *Phys. Rev. A* **73**, 022505 (2006).
- [46] J. E. Sansonetti, *J. Phys. Chem. Ref. Data* **35**, 301 (2006).
- [47] M. S. Safronova and U. I. Safronova, *Phys. Rev. A* **83**, 052508 (2011).
- [48] A. Reinhard, T. C. Liebisch, B. Knuffman, and G. Raithel, *Phys. Rev. A* **75**, 032712 (2007).
- [49] M. Marinescu, H. R. Sadeghpour, and A. Dalgarno, *Phys. Rev. A* **49**, 982 (1994).
- [50] N. Šibalić, J. D. Pritchard, C. S. Adams, and K. J. Weatherill, *Comput. Phys. Commun.* **220**, 319 (2017).
- [51] See Supplemental Material at <http://link.aps.org/supplemental/10.1103/PhysRevA.104.063304> for details on stabilizing the TEM00 lattice mode throughout the experiment, frequency control of the 795-nm and 762-nm probe lasers, and a numerical simulation of the experiment. Also See Refs. [28,37,40,41,52–54].
- [52] D. A. Steck, Rubidium 85 D line data, available online at <https://steck.us/alkalidata/> (revision 2021).
- [53] R. W. P. Drever, J. L. Hall, F. V. Kowalski, J. Hough, G. M. Ford, A. J. Munley, and H. Ward, *Appl. Phys. B* **31**, 97 (1983).
- [54] E. D. Black, *Am. J. Phys.* **69**, 79 (2001).
- [55] A. Duspayev, X. Han, M. A. Viray, L. Ma, J. Zhao, and G. Raithel, *Phys. Rev. Res.* **3**, 023114 (2021).
- [56] K. C. Younge, S. E. Anderson, and G. Raithel, *New J. Phys.* **12**, 023031 (2010).
- [57] R. Cardman, J. L. MacLennan, S. E. Anderson, Y.-J. Chen, and G. A. Raithel, *New J. Phys.* **23**, 063074 (2021).
- [58] J. C. Tully and R. K. Preston, *J. Chem. Phys.* **55**, 562 (1971).
- [59] J. C. Tully, *J. Chem. Phys.* **93**, 1061 (1990).